Nuclear Quantum Effects and the Grotthuss Mechanism Dictate the pH of Liquid Water

S. Dasgupta[1,*], G. Cassone[2], and F. Paesani[1,3,4,5,*]

[1]*Department of Chemistry and Biochemistry, University of California, San Diego, La Jolla, California 92093, United States*

[2]*Institute for Chemical-Physical Processes, National Research Council of Italy (IPCF-CNR), 98158 Messina, Italy*

[3]*Materials Science and Engineering, University of California San Diego, La Jolla, California 92093, United States*

[4]*Halıcıoğlu Data Science Institute, University of California San Diego, La Jolla, California 92093, United States*

[5]*San Diego Supercomputer Center, University of California San Diego, La Jolla, California 92093, United States*

[*]*email: s1dasgupta@ucsd.edu, fpaesani@ucsd.edu*

Abstract

Water's ability to autoionize into hydronium (H_3O^+) and hydroxide (OH^-) ions dictates the acidity or basicity of aqueous solutions, influencing the reaction pathways of many chemical and biochemical processes. In this study, we determine the molecular mechanism of the autoionization process by leveraging both the computational efficiency of a deep neural network potential trained on highly accurate data calculated within density-corrected density functional theory and the ability of enhanced

sampling techniques to ensure a comprehensive exploration of the underlying multidimensional free-energy landscape. By properly accounting for nuclear quantum effects, our simulations provide an accurate estimate of autoionization constant of liquid water ($pK_{\mathrm{w}} = 13.71 \pm 0.16$), offering a realistic molecular-level picture of the autoionization process and emphasizing its quantum-mechanical nature. Importantly, our simulations highlight the central role played by the Grotthuss mechanism in stabilizing solvent-separated ion pair configurations, revealing its profound impact on acid-base equilibria in aqueous environments.

Water is the most fundamental and ubiquitous substance on Earth, often referred to as the matrix of life.[1,2] Its unique behavior stems from two key features: the propensity to form fluctuating, extensive hydrogen-bond networks, and the ability to dissociate into hydronium (H_3O^+) and hydroxide (OH^-) ions. H_3O^+ and OH^- ions, also known as water's self-ions, modulate the solution's acidity/basicity, which is quantified in units of $pH = -\log[H_3O^+]$, where $[H_3O^+]$ is the hydronium concentration. The pH of a solution governs reaction pathways and rates by influencing molecular interactions and transformations, making a detailed understanding of the autoionization process essential for characterizing molecular mechanisms in various aqueous chemical and biochemical processes.[3–8] In bulk water, hydronium and hydroxide ions are stabilized by surrounding water molecules, creating structural defects in the underlying hydrogen-bond network.[9] The hydrated H_3O^+ ion can organize into various local arrangements, with Eigen ($H_9O_4^+$)[10] and Zundel ($H_5O_2^+$)[11] complexes generally considered as two of the primary limiting structures. These local protonated structures are dynamic, enabling rapid proton diffusion across the hydrogen-bond network via the Grotthuss mechanism.[12–21] In contrast, the hydrated hydroxide ion is highly fluxional,

adopting various local arrangements due to the diffuse excess electron density forming a "ring" around the oxygen atom, which lies in a plane perpendicular to the OH bond.[22–25] In liquid water at ambient conditions, the recombination of H_3O^+ and OH^- ions occurs significantly faster than proton diffusion,[26] directly correlating with their relatively low concentrations ($[H_3O^+] = [OH^-] = 10^{-7}$ M) and the correspondingly small equilibrium constant $K_w = [H_3O^+][OH^-] = 10^{-14}$, known as the autoionization constant of water.

While ultrafast vibrational spectroscopy has shed light on proton transport in aqueous acidic solutions,[14,18–21] gaining direct experimental insights into the autoionization process remains challenging. The challenge arises because the autoionization of a water molecule is a rare event, occurring on time scales of several hours.[27–29] In this context, computer simulations can play a central role by directly probing the thermodynamics and kinetics of water's autoionization at the molecular level. However, they face challenges such as accurately modeling reactive processes, efficient sampling of rare events, and accounting for nuclear quantum effects (NQEs). In particular, common force fields enable large scale molecular dynamics (MD) simulations of million-atom systems but fall short at describing chemical transformations as they generally do not allow molecules to form and break bonds. On the other hand, *ab initio* molecular dynamics (AIMD) simulations[30] and machine-learning potentials (MLP)[31] based on density functional theory (DFT)[32,33] allow for modeling the rearrangement of chemical bonds. While these methods are powerful, the density-functional approximations they rely on are typically hindered by functional-driven and density-driven errors.[34–37] These errors significantly impact the accuracy of AIMD and MLP-based simulations when modeling aqueous systems.[38–40] In particular, AIMD and MLP-based simulations are

commonly performed using semi-local functionals derived from the generalized gradient approximation (GGA functionals) and its improved variant, the meta-generalized gradient approximation (meta-GGA functionals). However, GGA and meta-GGA functionals have been shown to exhibit artificially strong hydrogen-bond networks due to spurious charge transfer contributions arising from delocalization errors.[40,41] These functionals, therefore, tend to overestimate the dissociative character of water. In this regard, it should be noted that classical AIMD simulations performed with GGA and meta-GGA functionals may sometimes predict pK_{w} values close to 14.[42–45] However, when NQEs are properly accounted for in analogous AIMD simulations performed using path-integral methods, water molecules display an unphysically high propensity to dissociate, resulting in pK_{w} values lower than 14.[44] As a consequence, although various DFT-based models have been used to investigate the autoionization process in liquid water, a realistic estimate of K_{w}, which accounts for a rigorous description of both underlying Born-Oppenheimer potential energy surface and NQEs, remain elusive.[42–54]

Recent studies have demonstrated the capability of *ab initio* models developed within the density-corrected DFT (DC-DFT) formalism,[35,55,56] which extends beyond conventional Kohn-Sham theory, to accurately simulate aqueous-phase chemistry.[38,40,57–60] In particular, it has been shown that DC-SCAN,[38,58,61,62] a density-corrected version of the SCAN functional,[63] achieves similar accuracy to the coupled cluster method, including single, double, and perturbative triple excitation, i.e., CCSD(T),[64,65] which is considered the current "gold standard" for chemical accuracy.[66,67] While DC-SCAN offers greater accuracy than SCAN, AIMD simulations with DC-SCAN are computationally expensive, requiring the calculation of the Hartree-Fock exchange term as well as the

solution of costly coupled-perturbed Kohn-Sham equations.[59,68,69]

Building upon the accuracy achieved by DC-SCAN for aqueous systems, we introduce here a deep neural network potential (DNN@DC-r^{2}SCAN) trained on reference data calculated at the DC-r^{2}SCAN level of theory[70] (see Methods for details). The accuracy and high computational efficiency of the DNN@DC-r^{2}SCAN potential enable realistic MD simulations of the autoionization process in liquid water by explicitly accounting for NQEs, a key factor often overlooked in computational studies. The combination of an accurate representation of the underlying Born-Oppenheimer potential energy surface and a correct treatment of molecular motion at the quantum-mechanical level enables a realistic modeling of K_{w} at the molecular level.

Results and Discussion

Free-energy landscape of water's autoionization. Given that the autoionization process in liquid water is a rare event occurring on timescales far exceeding those feasible for current MD simulations, we employed enhanced sampling methods, including umbrella sampling[71,72] and well-tempered metadynamics,[73] to monitor the formation of H_3O^+ and OH^- ions in water. These enhanced sampling simulations allowed for efficient exploration of the relevant free-energy landscape by inducing the dissociation of a water molecule through the application of a biasing potential along an appropriate collective variable describing the autoionization process. We then determined K_{w} from the free-energy difference between the undissociated (neutral water molecules) and dissociated (hydronium and hydroxide ions) states of water. All simulations were carried out with the DNN@DC-r^{2}SCAN potential for a periodic system containing 256 water molecules (see

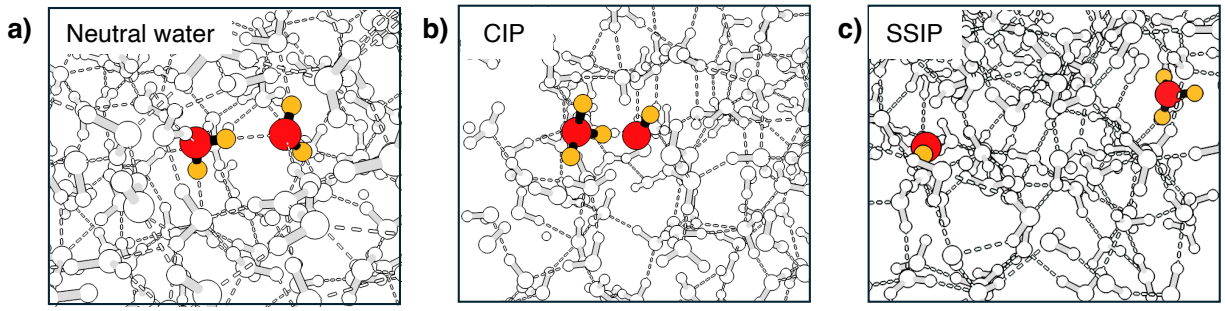

Figure 1: **Molecular structures involved in the autoionization process of liquid water.** **a**, Neutral water. **b**, Contact ion-pair (CIP). **c**, Solvent-separated ion pair (SSIP).

Methods for details).

The autoionization event of a water molecule results in the formation of a hydroxide ion and a proton, which promptly transfers to the nearest hydrogen-bonded molecule, forming a hydronium ion. This hydronium ion is highly dynamic, with the excess proton continuously hopping from one water molecule to another, causing the hydronium ion to constantly change its identity. Proton diffusion across the hydrogen-bond network of water, described by the Grotthuss mechanism,[12–21,74] causes the proton to move away from the hydroxide ion, resulting in the formation of a stable solvent-separated ion pair (SSIP) where the hydronium and hydroxide ions are separated by one or more water molecules. As illustrated in Figure 1, the autoionization of a water molecule involves two limiting structures, corresponding to neutral water and SSIP configurations, respectively, which are connected by contact-ion pair (CIP) configurations.

The free-energy landscape associated with the autoionization of a water molecule can be mapped into a two-dimensional space using the number of covalent bonds (n_{cov}) of the dissociating

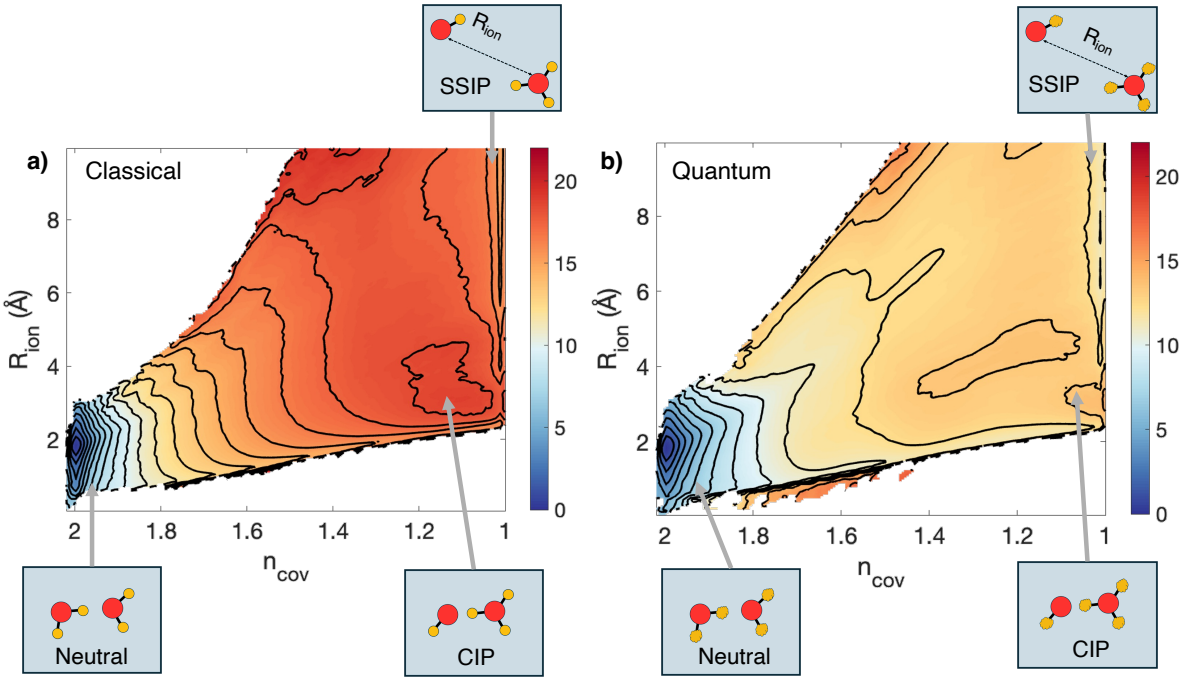

Figure 2: **Free-energy landscape of water's autoionization.** Two-dimensional free-enery surface (in kcal/mol) representing the autoionization process in liquid water as a function of covalent OH bonds (n_{cov}) of the self-dissociating molecule and the distance (R_{ion}) between the resulting H_3O^+ and OH^- ions. **a**, **b** Classical and quantum free-energy surfaces, respectively. Contour lines are drawn every 1 kcal/mol.

water molecule and the distance (R_{ion}) between the resulting H_3O^+ and OH^- ions as collective variables (Figure 2). The value of n_{cov} directly reports on the dissociation state, with $n_{\mathrm{cov}} = 1.0$ denoting the dissociated species (i.e., OH^-) and $n_{\mathrm{cov}} = 2.0$ corresponding to the undissociated species (i.e., H_2O). The distance R_{ion} allows for classifying the dissociated state in terms of well-defined molecular configurations. Specifically, $R_{\mathrm{ion}} \sim 2.8$ Å indicates CIP configurations, while larger R_{ion} values correspond to SSIP configurations.

As shown in Figure 2a, the two-dimensional free-energy landscape obtained from classical MD simulations indicates a free-energy difference of 14.93 ± 0.08 kcal/mol between the SSIP and neutral water configurations. Figure 2b shows that accounting for NQEs does not change the overall shape of the free-energy landscape, which however becomes significantly shallower. In particular, quantum simulations with the DNN@DC-r^{2}SCAN potential predict relatively more stable SSIP (10.99 ± 0.11 kcal/mol) and CIP (13.01 ± 0.19 kcal/mol) configurations relative to neutral water. Additional details are reported in Figure S10 of the Supplementary Information. Both classical and quantum free-energy landscapes indicate that the recombination of H_3O^+ and OH^- ions along the pathway connecting SSIP and neutral water configurations requires overcoming a barrier, corresponding to the location of CIP configurations. Partial Hessian normal-mode analysis[75–77] indicates that CIP configurations, where the H_3O^+ and OH^- ions are adjacent, effectively serve as transition states for the autoionization process (see Section 5 of the Supplementary Information). Classical and quantum simulations with the DNN@DC-r^{2}SCAN potential predict a barrier of $\sim$2.47 $\pm$ 0.06 kcal/mol and $\sim$2.02 $\pm$ 0.22 kcal/mol, respectively, indicating that the recombination reaction occurs on a picosecond timescale.[26,44] As shown in Figure S15 of the Supplementary Information these values are converged with respect to the system size. Experimentally, the recombination reaction barrier was estimated to be within 3 kcal/mol,[27] supporting the reliability of the present simulations with the DNN@DC-r^{2}SCAN potential. The barrier predicted by the DNN@DC-r^{2}SCAN potential for the recombination reaction is also comparable with the barriers associated with proton-transfer reactions in liquid water, as determined from analyses of NMR[78] and ultrafast infrared spectra.[79]

To calculate K_{w}, it is necessary to compute the free-energy change associated with separating the H_3O^+ and OH^- ions to an infinite distance. However, due to the periodic boundary conditions, it is not possible to reach an infinite separation between the H_3O^+ and OH^- ions in actual MD simulations. In practice, this free-energy change can be calculated from the corresponding Coulomb interaction energy, assuming that the H_3O^+ and OH^- ions can be represented as $+1$ and -1 point charges, respectively.[43–45] By performing umbrella sampling simulations over the $H_3O^+ \cdots OH^-$ distance at both classical and quantum levels, we determined an average distance, $\langle R_{\mathrm{ion}} \rangle$, of approximately 6.01 Å and 5.98 Å, respectively. $\langle R_{\mathrm{ion}} \rangle$ was then used to calculate the electrostatic Coulombic correction, which was added to the free-energy change to account for ion-pair separation at an infinite distance. In these configurations, the H_3O^+ and OH^- ions are separated by two water molecules. It should be noted that the compression of this $H_3O^+ \cdots H_2O \cdots H_2O \cdots OH^-$ water wire has been shown to lead to the recombination of the H_3O^+ and OH^- ions into neutral water via a concerted mechanism.[26,44] Starting from a SSIP configuration, we determined a free-energy change of 0.71 kcal/mol and 0.72 kcal/mol for the transition to infinitely separated point charges at the classical and quantum levels, respectively. Finally, the value of K_{w} was calculated from the free-energy changes associated with the autoionization of a water molecule and the separation of the H_3O^+ and OH^- ions to an infinite distance, accounting for standard state concentrations.[45,51,80]

Classical simulations with the DNN@DC-r^{2}SCAN potential predict $pK_{\mathrm{w}} = 19.44 \pm 0.11$. This corresponds to an equilibrium concentration of 1.91×10^{-10} M for both hydronium and hydroxide ions, which is approximately 500 times lower than the experimental concentration of these two ions in liquid water at ambient conditions (10^{-7} M). In contrast, quantum simulations with

the DNN@DC-r^{2}SCAN potential predict $pK_{\mathrm{w}} = 13.71 \pm 0.16$, which is in excellent agreement with the experimental value ($pK_{\mathrm{w}} = 14$). For heavy water (D_2O), the reduction in ZPE due to the heavier mass of the deuterium atoms leads to a decrease in NQEs. Consequently, D_2O exhibits properties that lie between those of classical H_2O and quantum H_2O, with an experimental pK_{w} value of 14.86.[81] Figure S16 indicates that the free-energy profile associated with the autoionization reaction in liquid D_2O is intermediate between those obtained from classical and quantum simulations of liquid H_2O, aligning with the expected behavior based on the reduced ZPE and NQEs in liquid D_2O. The free-energy difference of 12.02 $\pm$ 0.20 kcal/mol calculated for liquid D_2O corresponds to $pK_{\mathrm{w}} = 15.07 \pm 0.30$, which is in close agreement with the experimental value. The difference between the pK_{w} values calculated from classical and quantum simulations of H_2O and D_2O with the DNN@DC-r^{2}SCAN potential unambiguously demonstrates the quantum nature of the autoionization process in liquid water. These results are consistent with analyses reported for liquid water under electric fields.[82]

Hydrogen-bonding topologies and water's autoionization. Further insights into the autoionization process are gained from the analysis of the evolution of the local hydrogen-bonding topologies as a water molecule dissociates into its self-ions. In liquid water at ambient conditions, every molecule, on average, participates in four hydrogen bonds, each accepting and donating two hydrogen bonds, *i.e.*, $n_{\mathrm{HB(D)}} \approx 2$ and $n_{\mathrm{HB(A)}} \approx 2$, respectively. During the autoionization event, Figure 3a shows that the dissociating water molecule progressively decreases its number of covalent OH bonds (n_{cov}) by transferring a proton to the closest hydrogen-bonded molecule. As the proton is transferred, this molecule gradually transforms into a nascent hydroxide ion, a change reflected

in the value of n_{cov} progressively decreasing from 2.0 to 1.0. Figure 3 shows that, in its limiting dissociated structure ($n_{\mathrm{cov}} = 1.0$), the hydroxide ion, on average, accepts five hydrogen bonds (Figure S17 of the Supplementary Information), in agreement with previous MD simulations showing the tendency of OH^- to be hypercoordinated.[22,24,25] The increase from $n_{\mathrm{HB(A)}} \approx 2$ to $n_{\mathrm{HB(A)}} \approx 5$ indicates the formation of a defect within the water hydrogen-bond network, with more water molecules preferentially donating hydrogen bonds to the hydroxide ion.[26,42,47] It should be noted that, within a CIP configuration, one of the hydrogen bonds accepted by the nascent hydroxide ion is donated by the nascent hydronium ion. Figure 3b also demonstrates that the incorporation of NQEs tends to further delocalize the transferring proton. This is evidenced by the relatively larger percentage of $n_{\mathrm{HB(A)}}$ for configurations where the proton is equally shared between the

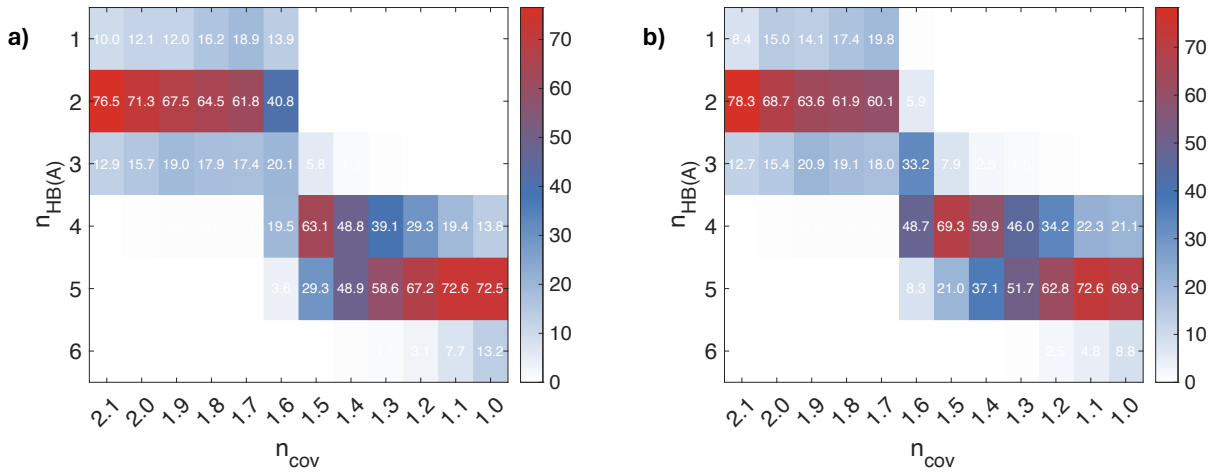

Figure 3: **Changes in hydrogen-bonding topologies during the autoionization process.** Matrix showing the percentage of hydrogen bonds (n_{HB}) relative to the number of covalent bonds (n_{cov}) of the self-dissociating water molecule. **a**, **b**, Results from classical and quantum MD simulations, respectively.

nascent hydronium and hydroxide species ($n_{\mathrm{cov}} = 1.5 - 1.6$) compared to the corresponding values obtained from classical simulations. These differences in hydrogen-bonding environment thus explain the relatively higher acidity of "quantum" water compared to "classical" water, which is directly reflected in the higher K_{w} value as a consequence of the more diffuse nature of the transferring proton. Both classical and quantum simulations indicate that the autoionization process does not occur until the distance between the oxygen atom of the dissociating water molecule and its transferring proton (H^*) remains between 0.97 and 1.30 Å (Figure S18 of the Supplementary Information). When the distance of H^* from the oxygen atoms of the nascent hydronium (O_A) and hydroxide (O_D) ions is between 1.34 and 1.37 Å, H^* is equally shared by the two ions, which corresponds to configurations with $n_{\mathrm{cov}} = 1.5 - 1.6$. When the distance between O_D and H^* exceeds 1.45 Å, the number of covalent OH bonds drastically changes for both ions, signaling the formation of well-defined CIP configurations (Figure S19 of the Supplementary Information).

Grotthuss mechanism and water's autoionization. As time progresses, the excess proton on the hydronium ion within the initial CIP configuration hops through the hydrogen-bond network, leading to the formation of stable SSIP configurations. In these configurations, $R_{O_D H^*} - R_{O_A H^*} > 3$ Å, where O_A and O_D now define the oxygen atoms of the stable hydronium and hydroxide ions (Figure 4a). To assess the role played by the Grotthuss mechanism on the thermodynamics of the autoionization process, we performed MD simulations where proton transfer was only allowed between two labeled water molecules, with the rest of the water acting as passive spectators (Figure 4b). Figure 4c shows that suppressing proton hopping through the underlying hydrogen-bond network in the classical simulations leads to a significant increase in the free energy associated with

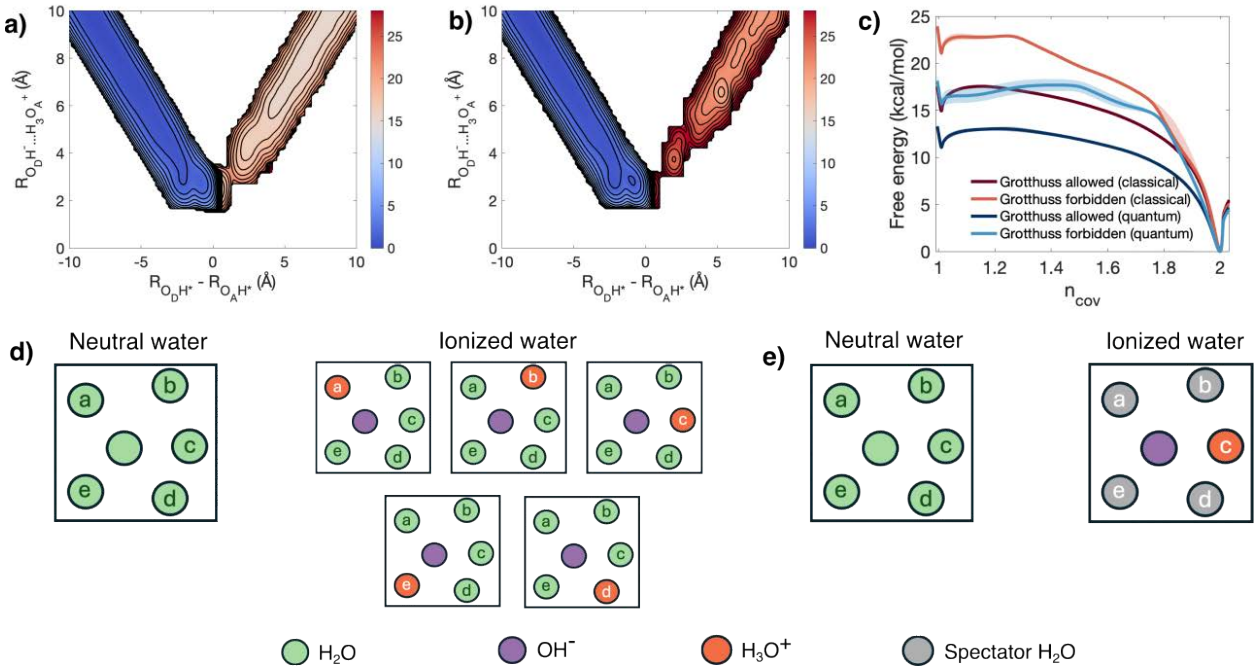

Figure 4: **Effect of the Grotthuss mechanism on the autoionization of water.** **a**, **b**, Two-dimensional free-energy surface of water's autoionization calculated from classical simulations with the Grotthuss mechanism allowed and suppressed, respectively. $R_{\mathrm{O_DH^*}} - R_{\mathrm{O_AH^*}}$ on the x-axis defines the proton transfer coordinate and $R_{\mathrm{OH^-\cdots H_3O^+}}$ on the y-axis defines the oxygen–oxygen distance between the hydroxide and hydronium ions. **c**, Comparison between classical and quantum free-energy changes from neutral water ($n_{\mathrm{cov}} = 2$) to SSIP ($n_{\mathrm{cov}} = 1$) configurations calculated from simulations with both the Grotthuss mechanism allowed and forbidden. **d,e**, Schematic representation of neutral and ionized water with Grotthuss-allowed and Grotthuss-forbidden mechanisms, respectively.

SSIP configurations (21.29 ± 0.03 kcal/mol) compared to the corresponding value obtained when the Grotthuss mechanism is allowed (14.93 ± 0.08 kcal/mol). Explicitly accounting for NQEs qualitatively provides the same trends in the free-energy change from neutral water ($n_{\mathrm{cov}} = 2$) to SSIP

($n_{\mathrm{cov}} = 1$) configurations, with the latter being destabilized by 4.64 kcal/mol when the Grotthuss mechanism is suppressed. Without proton hopping, the formation of stable SSIP configurations requires the diffusion of both hydronium and hydroxide ions. This process necessitates continuous rearrangements of the surrounding hydrogen-bond network, which adds an energetic penalty. Additionally, in the Grotthuss-allowed mechanism, a proton can hop between several water molecules in the dissociated SSIP state, resulting in a larger number of possible configurations (Figure 4d). Each of these accessible configurations increases the entropy of the dissociated state, making it more stable. In contrast, in the Grotthuss-forbidden mechanism, proton transfer occurs only between a pair of water molecules, resulting in relatively lower entropy for the dissociated state due to the reduced number of possible configurations (Figure 4e). Thus, the entropic effects introduced by the Grotthuss mechanism play a crucial role in stabilizing the SSIP state, significantly influencing the thermodynamics of the autoionization process. This analysis implies that, without the Grotthuss mechanism, K_{w} would be significantly smaller, which may have implications for acid-base equilibria in aqueous environments where proton diffusion is suppressed.

Discussion

In this study, we have introduced a deep neural network potential (DNN@DC-r^{2}SCAN) trained on accurate data for both neutral and dissociated water, calculated at the DC-r^{2}SCAN level of theory, which enables realistic MD simulations of the autoionization process in liquid water. By combining enhanced sampling techniques, which ensure a comprehensive exploration of the underlying multidimensional free-energy landscape, with a proper treatment of nuclear quantum effects, our

simulations predict a pK_{w} value of 13.71 ± 0.16, in excellent agreement with the experimental value ($pK_{\mathrm{w}} = 14.00$). Importantly, upon isotopic substitution, our quantum simulations predict a pK_{w} value of 15.07 ± 0.30 for liquid D_2O, which is in close agreement with the experimental value of 14.86, further supporting the ability of the DNN@DC-r^{2}SCAN potential to accurately represent the underlying Born-Oppenheimer surface of water. This agreement between experiment and simulation establishes a realistic molecular-level picture of the mechanistic steps involved in the autoionization process. Detailed analyses of the evolution of hydrogen-bonding topologies during the autoionization process indicate that nuclear quantum effects lower the free energy of contact-ion pair (CIP) configurations, which effectively serve as transition states along the pathway connecting neutral water molecules to solvent-separated ion pair (SSIP) configurations. Importantly, our simulations reveal that the Grotthuss mechanism plays a critical role in stabilizing SSIP configurations and, consequently, determining the value of K_{w}. These findings indicate that the thermodynamics of the autoionization process may be altered in aqueous environments where the Grotthuss mechanism is inhibited, which can, in turn, impact acid-base equilibria in those systems.

Methods

The DNN@DC-r^{2}SCAN potential was trained within the DeePMD framework[83] on extensive datasets for neutral and autoionized water calculated at the DC-r^{2}SCAN level.[70] Although DeePMD-based potentials for water do not precisely replicate their parent models,[84,85] they offer robust representations for specific properties when trained on relevant regions of the configuration space,[86] as done in this study for modeling water autoionization. Specific details about the development and

validation of the DNN@DC-r^{2}SCAN potential are discussed in the Supplementary Information.

The simulations were carried out using LAMMPS[87] patched with PLUMED[88,89] and DeePMD-kit [83] for a system consisting of 256 water molecules in periodic boundary conditions. Nuclear quantum effects were incorporated using the path-integral generalized Langevin equation thermostat (PIGLET) method[90] as implemented in i-PI.[91] All simulations were conducted at 300 K in the canonical (NVT: constant number of molecules, volume, temperature) ensemble, with the temperature controlled by a global Nosé-Hoover thermostat.[92–95] The equations of motion were propagated using the velocity-Verlet algorithm.[96,97] Umbrella sampling[71,72] and well-tempered metadynamics[73] simulations were performed to characterize the free-energy landscape associated with the autoionization process. In the classical case, the umbrella sampling simulations were carried out for 2 ns for each window, using a time step of 0.5 fs. In the quantum case, the umbrella sampling simulations were carried out for 1 ns for each window, using a time step of 0.1 fs. Well-tempered metadynamics simulations were carried out for 40 ns. Specific details about all MD simulations and numerical analyses are presented in the Supplementary Information.

Data availability

All DNN@DC-r^{2}SCAN MD trajectories are available from the authors upon request. The DNN@DC-r^{2}SCAN potential, along with the corresponding training set, is publicly available on GitHub at: https://github.com/-paesanilab/Data_Repository/tree/main/DC-r2SCAN_water_autoionization%20.

Code availability

All DNN@DC-r^{2}SCAN MD simulations were carried out with LAMMPS[87] and i-PI[91] patched with the DeePMD-kit plugin.[83]

References

1. Franks, F. *Water: A matrix of life*, vol. 21 (Royal Society of Chemistry, 2000).

2. Ball, P. *Life's Matrix: A biography of water* (Univ of California Press, 2001).

3. Hynes, J. T. Chemical reaction dynamics in solution. *Annu. Rev. Phys. Chem.* **36**, 573–597 (1985).

4. Vácha, R., Buch, V., Milet, A., Devlin, J. P. & Jungwirth, P. Autoionization at the surface of neat water: Is the top layer pH neutral, basic, or acidic? *Phys. Chem. Chem. Phys.* **9**, 4736–4747 (2007).

5. Hu, H. & Yang, W. Free energies of chemical reactions in solution and in enzymes with *ab initio* quantum mechanics/molecular mechanics methods. *Annu. Rev. Phys. Chem.* **59**, 573–601 (2008).

6. Tournaire-Roux, C. *et al.* Cytosolic pH regulates root water transport during anoxic stress through gating of aquaporins. *Nature* **425**, 393–397 (2003).

7. Hoffmann, E. K. & Simonsen, L. Membrane mechanisms in volume and pH regulation in vertebrate cells. *Physiol. Rev.* **69**, 315–382 (1989).

8. Pye, H. O. *et al.* The acidity of atmospheric particles and clouds. *Atmos. Chem. Phys.* **20**, 4809–4888 (2020).

9. Agmon, N. *et al.* Protons and hydroxide ions in aqueous systems. *Chem. Rev.* **116**, 7642–7672 (2016).

10. Eigen, M. Proton transfer, acid-base catalysis, and enzymatic hydrolysis. Part I: Elementary processes. *Angew. Chem. Int. Ed.* **3**, 1–19 (1964).

11. Zundel, G. & Metzger, H. Energiebänder der tunnelnden überschuß-protonen in flüssigen säuren. eine ir-spektroskopische untersuchung der natur der gruppierungen $H_5O_2^+$. *Z. Phys. Chem.* **58**, 225–245 (1968).

12. De Grotthuss, C. *Mémoire Sur la Décomposition de L'eau: et Des Corps Qu'elle Tient en Dissolution à L'aide de L'électricité Galvanique* (1805).

13. Agmon, N. The Grotthuss mechanism. *Chem. Phys. Lett.* **244**, 456–462 (1995).

14. Mohammed, O. F., Pines, D., Dreyer, J., Pines, E. & Nibbering, E. T. Sequential proton transfer through water bridges in acid-base reactions. *Science* **310**, 83–86 (2005).

15. Marx, D. Proton transfer 200 years after von Grotthuss: Insights from *ab initio* simulations. *ChemPhysChem* **7**, 1848–1870 (2006).

16. Markovitch, O. *et al.* Special pair dance and partner selection: Elementary steps in proton transport in liquid water. *J. Phys. Chem. B* **112**, 9456–9466 (2008).

17. Knight, C. & Voth, G. A. The curious case of the hydrated proton. *Acc. Chem. Res.* **45**, 101–109 (2012).

18. Thämer, M., De Marco, L., Ramasesha, K., Mandal, A. & Tokmakoff, A. Ultrafast 2D IR spectroscopy of the excess proton in liquid water. *Science* **350**, 78–82 (2015).

19. Dahms, F. *et al.* The hydrated excess proton in the Zundel cation $H_5O_2^+$: The role of ultrafast solvent fluctuations. *Angew. Chem. Int. Ed.* **55**, 10600–10605 (2016).

20. Dahms, F., Fingerhut, B. P., Nibbering, E. T., Pines, E. & Elsaesser, T. Large-amplitude transfer motion of hydrated excess protons mapped by ultrafast 2D IR spectroscopy. *Science* **357**, 491–495 (2017).

21. Fournier, J. A., Carpenter, W. B., Lewis, N. H. & Tokmakoff, A. Broadband 2D IR spectroscopy reveals dominant asymmetric $H_5O_2^+$ proton hydration structures in acid solutions. *Nat. Chem.* **10**, 932–937 (2018).

22. Tuckerman, M. E., Marx, D. & Parrinello, M. The nature and transport mechanism of hydrated hydroxide ions in aqueous solution. *Nature* **417**, 925–929 (2002).

23. Aziz, E. F., Ottosson, N., Faubel, M., Hertel, I. V. & Winter, B. Interaction between liquid water and hydroxide revealed by core-hole de-excitation. *Nature* **455**, 89–91 (2008).

24. Roberts, S. T. *et al.* Observation of a Zundel-like transition state during proton transfer in aqueous hydroxide solutions. *Proc. Natl. Acad. Sci. U.S.A.* **106**, 15154–15159 (2009).

25. Chen, M. *et al.* Hydroxide diffuses slower than hydronium in water because its solvated structure inhibits correlated proton transfer. *Nat. Chem.* **10**, 413–419 (2018).

26. Hassanali, A., Prakash, M. K., Eshet, H. & Parrinello, M. On the recombination of hydronium and hydroxide ions in water. *Proc. Natl. Acad. Sci. USA* **108**, 20410–20415 (2011).

27. Eigen, M. & De Maeyer, L. Untersuchungen über die kinetik der neutralisation. I. *Ber. Bunsenges. Phys. Chem.* **59**, 986–993 (1955).

28. Eigen, M. & De Maeyer, L. Self-dissociation and protonic charge transport in water and. *Proc. R. Soc. A: Math. Phys. Eng. Sci.* **247**, 505–533 (1958).

29. Natzle, W. C. & Moore, C. B. Recombination of hydrogen ion (H^+) and hydroxide in pure liquid water. *J. Phys. Chem.* **89**, 2605–2612 (1985).

30. Car, R. & Parrinello, M. Unified approach for molecular dynamics and density-functional theory. *Phys. Rev. Lett.* **55**, 2471 (1985).

31. Behler, J. Perspective: Machine learning potentials for atomistic simulations. *J. Chem. Phys.* **145** (2016).

32. Hohenberg, P. & Kohn, W. Inhomogeneous electron gas. *Phys. Rev.* **136**, B864 (1964).

33. Kohn, W. & Sham, L. J. Self-consistent equations including exchange and correlation effects. *Phys. Rev.* **140**, A1133 (1965).

34. Johnson, E. R., Mori-Sánchez, P., Cohen, A. J. & Yang, W. Delocalization errors in density functionals and implications for main-group thermochemistry. *J. Chem. Phys.* **129** (2008).

35. Vuckovic, S., Song, S., Kozlowski, J., Sim, E. & Burke, K. Density functional analysis: The theory of density-corrected DFT. *J. Chem. Theory Comput.* **15**, 6636–6646 (2019).

36. Song, S., Vuckovic, S., Sim, E. & Burke, K. Density-corrected DFT explained: Questions and answers. *J. Chem. Theory Comput.* **18**, 817–827 (2022).

37. Sim, E., Song, S., Vuckovic, S. & Burke, K. Improving results by improving densities: Density-corrected density functional theory. *J. Am. Chem. Soc.* **144**, 6625–6639 (2022).

38. Dasgupta, S., Lambros, E., Perdew, J. & Paesani, F. Elevating density functional theory to chemical accuracy for water simulations through a density-corrected many-body formalism. *Nat. Commun.* **12**, 1–12 (2021).

39. Lambros, E., Hu, J. & Paesani, F. Assessing the accuracy of the SCAN functional for water through a many-body analysis of the adiabatic connection formula. *J. Chem. Theory Comput.* **17**, 3739–3749 (2021).

40. Palos, E. *et al.* Assessing the interplay between functional-driven and density-driven errors in DFT models of water. *J. Chem. Theory Comput.* **18**, 3410–3426 (2022).

41. Dasgupta, S., Palos, E., Pan, Y. & Paesani, F. Balance between physical interpretability and energetic predictability in widely used dispersion-corrected density functionals. *J. Chem. Theory Comput.* **20**, 49–67 (2024).

42. Geissler, P. L., Dellago, C., Chandler, D., Hutter, J. & Parrinello, M. Autoionization in liquid water. *Science* **291**, 2121–2124 (2001).

43. Wang, R., Carnevale, V., Klein, M. L. & Borguet, E. First-principles calculation of water pK_a using the newly developed scan functional. *J. Phys. Chem. Lett.* **11**, 54–59 (2019).

44. Liu, L., Tian, Y., Yang, X. & Liu, C. Mechanistic insights into water autoionization through metadynamics simulation enhanced by machine learning. *Phys. Rev. Lett.* **131**, 158001 (2023).

45. Calegari Andrade, M., Car, R. & Selloni, A. Probing the self-ionization of liquid water with *Ab initio* deep potential molecular dynamics. *Proc. Natl. Acad. Sci. USA* **120**, e2302468120 (2023).

46. Sprik, M. Computation of the pK_a of liquid water using coordination constraints. *Chem. Phys.* **258**, 139–150 (2000).

47. Joutsuka, T. Molecular mechanism of autodissociation in liquid water: *Ab initio* molecular dynamics simulations. *J. Phys. Chem. B* **126**, 4565–4571 (2022).

48. Trout, B. L. & Parrinello, M. The dissociation mechanism of H_2O in water studied by first-principles molecular dynamics. *Chem. Phys. Lett.* **288**, 343–347 (1998).

49. Trout, B. L. & Parrinello, M. Analysis of the dissociation of H_2O in water using first-principles molecular dynamics. *J. Phys. Chem. B* **103**, 7340–7345 (1999).

50. Lan, J., Rybkin, V. V. & Iannuzzi, M. Ionization of water as an effect of quantum delocalization at aqueous electrode interfaces. *J. Phys. Chem. Lett.* **11**, 3724–3730 (2020).

51. Thomsen, B. & Shiga, M. Nuclear quantum effects on autoionization of water isotopologs studied by *ab initio* path integral molecular dynamics. *J. Chem. Phys.* **154**, 084117 (2021).

52. de la Puente, M. & Laage, D. How the acidity of water droplets and films is controlled by the air–water interface. *J. Am. Chem. Soc.* **145**, 25186–25194 (2023).

53. Zhang, P., Gardini, A. T. & Xu, X. Propensity of water self-ions at air (oil)-water interfaces revealed by deep potential molecular dynamics with enhanced sampling. *arXiv preprint arXiv:2404.07027* (2024).

54. Muñoz-Santiburcio, D. Precise and accurate determination of the pK_w of water via a new protocol within the blue moon ensemble. *ChemRxiv* (2024).

55. Scuseria, G. E. Comparison of coupled-cluster results with a hybrid of Hartree–Fock and density functional theory. *J. Chem. Phys.* **97**, 7528–7530 (1992).

56. Kim, M.-C., Sim, E. & Burke, K. Understanding and reducing errors in density functional calculations. *Phys. Rev. Lett.* **111**, 073003 (2013).

57. Lambros, E. *et al.* General many-body framework for data-driven potentials with arbitrary quantum mechanical accuracy: Water as a case study. *J. Chem. Theory Comput.* **17**, 5635–5650 (2021).

58. Dasgupta, S., Shahi, C., Bhetwal, P., Perdew, J. P. & Paesani, F. How good is the density-corrected scan functional for neutral and ionic aqueous systems and what is so right about the hartree-fock density? *J. Chem. Theory Comput.* **18**, 4745–4761 (2022).

59. Belleflamme, F. & Hutter, J. Radicals in aqueous solution: Assessment of density-corrected scan functional. *Phys. Chem. Chem. Phys.* **25**, 20817–20836 (2023).

60. Zhang, J., Pagotto, J., Gould, T. & Duignan, T. T. Accurate, fast and generalisable first principles simulation of aqueous lithium chloride. *arXiv preprint arXiv:2310.12535* (2023).

61. Song, S. *et al.* Extending density functional theory with near chemical accuracy beyond pure water. *Nat. Commun.* **14**, 799 (2023).

62. Palos, E., Caruso, A. & Paesani, F. Consistent density functional theory-based description of ion hydration through density-corrected many-body representations. *J. Chem. Phys.* **159**, 181101 (2023).

63. Sun, J., Ruzsinszky, A. & Perdew, J. P. Strongly constrained and appropriately normed semilocal density functional. *Phys. Rev. Lett.* **115**, 036402 (2015).

64. Purvis, G. D. & Bartlett, R. J. A full coupled-cluster singles and doubles model: The inclusion of disconnected triples. *J. Chem. Phys.* **76**, 1910–1918 (1982).

65. Bartlett, R. J. & Musiał, M. Coupled-cluster theory in quantum chemistry. *Rev. Mod. Phys.* **79**, 291–352 (2007).

66. Stanton, J. F. Why CCSD(T) works: A different perspective. *Chem. Phys. Lett.* **281**, 130–134 (1997).

67. Rezac, J. & Hobza, P. Benchmark calculations of interaction energies in noncovalent complexes and their applications. *Chem. Rev.* **116**, 5038–5071 (2016).

68. Verma, P., Perera, A. & Bartlett, R. J. Increasing the applicability of DFT I: Non-variational correlation corrections from Hartree–Fock DFT for predicting transition states. *Chem. Phys. Lett.* **524**, 10–15 (2012).

69. Rana, B., Coons, M. P. & Herbert, J. M. Detection and correction of delocalization errors for electron and hole polarons using density-corrected DFT. *J. Phys. Chem. Lett.* **13**, 5275–5284 (2022).

70. Furness, J. W., Kaplan, A. D., Ning, J., Perdew, J. P. & Sun, J. Accurate and numerically efficient r^{2}SCAN meta-generalized gradient approximation. *J. Phys. Chem. Lett.* **11**, 8208–8215 (2020).

71. Torrie, G. M. & Valleau, J. P. Nonphysical sampling distributions in monte carlo free-energy estimation: Umbrella sampling. *J. Comput. Phys.* **23**, 187–199 (1977).

72. Kästner, J. Umbrella sampling. *WIREs Comput. Mol. Sci.* **1**, 932–942 (2011).

73. Barducci, A., Bussi, G. & Parrinello, M. Well-tempered metadynamics: A smoothly converging and tunable free-energy method. *Phys. Rev. Lett.* **100**, 020603 (2008).

74. Di Pino, S. *et al.* ZundEig: The structure of the proton in liquid water from unsupervised learning. *J. Phys. Chem. B* **127**, 9822–9832 (2023).

75. Li, H. & Jensen, J. H. Partial Hessian vibrational analysis: The localization of the molecular vibrational energy and entropy. *Theor. Chem. Acc.* **107**, 211–219 (2002).

76. Besley, N. A. & Metcalf, K. A. Computation of the amide I band of polypeptides and proteins using a partial hessian approach. *J. Chem. Phys.* **126** (2007).

77. Bowling, P. E., Dasgupta, S. & Herbert, J. M. Eliminating imaginary vibrational frequencies in quantum-chemical cluster models of enzymatic active sites. *J. Chem. Inf. Model.* **64**, 3912–3922 (2024).

78. Luz, Z. & Meiboom, S. The activation energies of proton transfer reactions in water. *J. Am. Chem. Soc.* **86**, 4768–4769 (1964).

79. Carpenter, W. B., Lewis, N. H., Fournier, J. A. & Tokmakoff, A. Entropic barriers in the kinetics of aqueous proton transfer. *J. Chem. Phys.* **151**, 034501 (2019).

80. Chandler, D. Introduction to modern statistical mechanics. *Mechanics. Oxford University Press, Oxford, UK* **5**, 11 (1987).

81. Shoesmith, D. W. & Lee, W. The ionization constant of heavy water (D_2O) in the temperature range 298 to 523 K. *Can. J. Chem.* **54**, 3553–3558 (1976).

82. Cassone, G. Nuclear quantum effects largely influence molecular dissociation and proton transfer in liquid water under an electric field. *J. Phys. Chem. Lett.* **11**, 8983–8988 (2020).

83. Wang, H., Zhang, L., Han, J. & Weinan, E. DeePMD-kit: A deep learning package for many-body potential energy representation and molecular dynamics. *Comput. Phys. Commun.* **228**, 178–184 (2018).

84. Zhai, Y., Caruso, A., Bore, S. L., Luo, Z. & Paesani, F. A "short blanket" dilemma for a state-of-the-art neural network potential for water: Reproducing experimental properties or the physics of the underlying many-body interactions? *J. Chem. Phys.* **158**, 084111 (2023).

85. Zhai, Y., Rashmi, R., Palos, E. & Paesani, F. Many-body interactions and deep neural network potentials for water. *J. Chem. Phys.* **160**, 144501 (2024).

86. Bore, S. L. & Paesani, F. Realistic phase diagram of water from "first principles" data-driven quantum simulations. *Nat. Commun.* **14**, 3349 (2023).

87. Thompson, A. P. *et al.* LAMMPS – A flexible simulation tool for particle-based materials modeling at the atomic, meso, and continuum scales. *Comput. Phys. Commun.* **271**, 108171 (2022).

88. Tribello, G. A., Bonomi, M., Branduardi, D., Camilloni, C. & Bussi, G. PLUMED 2: New feathers for an old bird. *Comput. Phys. Commun.* **185**, 604–613 (2014).

89. Bonomi, M. *et al.* Promoting transparency and reproducibility in enhanced molecular simulations. *Nat. Methods* **16**, 670–673 (2019).

90. Ceriotti, M. & Manolopoulos, D. E. Efficient first-principles calculation of the quantum kinetic energy and momentum distribution of nuclei. *Phys. Rev. Lett.* **109**, 100604 (2012).

91. Kapil, V. *et al.* i-PI 2.0: A universal force engine for advanced molecular simulations. *Comput. Phys. Commun.* **236**, 214–223 (2019).

92. Nosé, S. A molecular dynamics method for simulations in the canonical ensemble. *Mol. Phys.* **52**, 255–268 (1984).

93. Nosé, S. A unified formulation of the constant temperature molecular dynamics methods. *J. Chem. Phys.* **81**, 511–519 (1984).

94. Hoover, W. G. Canonical dynamics: Equilibrium phase-space distributions. *Phys. Rev. A* **31**, 1695 (1985).

95. Martyna, G. J., Klein, M. L. & Tuckerman, M. Nosé–Hoover chains: The canonical ensemble via continuous dynamics. *J. Chem. Phys.* **97**, 2635–2643 (1992).

96. Swope, W. C., Andersen, H. C., Berens, P. H. & Wilson, K. R. A computer simulation method for the calculation of equilibrium constants for the formation of physical clusters of molecules: Application to small water clusters. *J. Chem. Phys.* **76**, 637–649 (1982).

97. Shinoda, W., Shiga, M. & Mikami, M. Rapid estimation of elastic constants by molecular dynamics simulation under constant stress. *Phys. Rev. B* **69**, 134103 (2004).

Acknowledgments

We thank Gareth Tribello for the assistance in implementing the collective variables with a development version of PLUMED and Jürg Hutter for the assistance in setting up exploratory *ab initio* calculations with the Harris functional using CP2K at an early stage of this work. We also thank Richa Rashmi for her help in setting up the quantum simulations with PIGLET and Sigbjörn Bore

for discussions regarding the development of DNN@DC-r^{2}SCAN. This research was supported by the National Science Foundation through grant no. 2311260. S.D. acknowledges support from the Eric and Wendy Schmidt AI in Science Postdoctoral Fellowship, a program of Schmidt Futures. Computational resources were provided by Advanced Cyberinfrastructure Coordination Ecosystem: Services & Support (ACCESS) program, which is supported by National Science Foundation grants nos. 2138259, 2138286, 2138307, 2137603, and 2138296, the Triton Shared Computing Cluster (TSCC) at the San Diego Supercomputer Center (SDSC), National Energy Research Scientific Computing Center (NERSC) supported by the Office of Science of the U.S. Department of Energy under Contract DE-AC02-05CH11231 and the Scientific Computing Core at the Flatiron Institute, a division of the Simons Foundation.

Author contributions

F.P. conceived the research. S.D. and F.P. designed the research. S.D. developed the DNN@DC-r^{2}SCAN potential and performed the simulations. G.C. provided configurations of ionized water and performed benchmark calculations. S.D. and F.P. analyzed the results and wrote the paper. S.D. and F.P. acquired funding. F.P. administered the project.

Competing interests

The authors declare no competing interests.

Additional information

Supplementary information. Details about the development and validation of the DNN@DC-r^{2}SCAN potentials, along with details about all MD simulations.